A reversible implantable memristor for health monitoring applications

Zelin Cao [a,b,c,d], Linbiao Xiang [a,b], Bai Sun [a,b,c,d,*], Kaikai Gao [a,b,c,d], Jiawei Yu [a,b], Guangdong Zhou [e], Xuegang Duan [c,d], Wentao Yan [c,d], Fulai Lin [a,b], Zhuoqun Li [a,b], Ruixin Wang [a], Yi Lv [a,b], Fenggang Ren [a,b], Yingmin Yao [f], Qiang Lu [f,g,**]

[a] National Local Joint Engineering Research Center for Precision Surgery & Regenerative Medicine, The First Affiliated Hospital of Xi'an Jiaotong University, Xi'an, Shaanxi, 710049, China
[b] Department of Hepatobiliary Surgery, The First Affiliated Hospital of Xi'an Jiaotong University, Xi'an, Shaanxi, 710049, China
[c] Micro-and Nano-technology Research Center, State Key Laboratory for Manufacturing Systems Engineering, Xi'an Jiaotong University, Xi'an, Shaanxi, 710049, China
[d] Frontier Institute of Science and Technology (FIST), Xi'an Jiaotong University, Xi'an, Shaanxi, 710049, China
[e] College of Artificial Intelligence, Brain-inspired Computing & Intelligent Control of Chongqing Key Lab, Southwest University, Chongqing, 400715, China
[f] Department of Geriatric Surgery, The First Affiliated Hospital of Xi'an Jiaotong University, Xi'an, Shaanxi, 710049, China
[g] National Local Joint Engineering Research Center for Precision Surgery & Regenerative Medicine, The First Affiliated Hospital of Xi'an Jiaotong University, Xi'an, Shaanxi, 710049, China

ARTICLE INFO

ABSTRACT

Conventional implantable electronics based on von Neumann architectures encounter significant limitations in computing and processing vast biological information due to computational bottlenecks. The memristor with integrated memory-computing and low power consumption offer a promising solution to overcome the computational bottleneck and Moore's law limitations of traditional silicon-based implantable devices, making them the most promising candidates for next-generation implantable devices. In this work, a highly stable memristor with an Ag/BaTiO$_3$/MnO$_2$/FTO structure was fabricated, demonstrating retention characteristics exceeding 1200 cycles and endurance above 1000 s. The device successfully exhibited three-stage responses to biological signals after implantation in SD (Sprague-Dawley) rats. Importantly, the memristor perform remarkable reversibility, maintaining over 100 cycles of stable repetition even after extraction from the rat. This study provides a new perspective on the biomedical application of memristors, expanding the potential of implantable memristive devices in intelligent medical fields such as health monitoring and auxiliary diagnostics.

1. Introduction

Over the years, advances in information technology as well as advances in medicine have led to a growing demand for implantable medical devices. Traditional implantable devices such as orthopedic prostheses [1], cardiovascular devices [2], ocular and cochlear implants [3], and tissue engineering scaffolds [4], are no longer able to meet the demands of the current information development. Digitization of devices in the medical industry has become a major trend in development. So far, a number of wearable and implantable devices have been proposed to monitor patient vital sign information such as blood glucose, blood pressure, etc. [5,6]. However, these devices do not have the ability to collect data in real time. At the same time, these digital devices

generate a large amount of data on patient's signs, which cannot be efficiently stored and processed by existing systems to accurately monitor the patient, which becomes one of the most problematic issues in realizing implantable monitoring [7].

Memristor is regarded as one of the most promising candidates to solve computing bottleneck problem of traditional von Neumann-based computing system due to its high operating speed, low power consumption, strong parallel computing ability and computing in memory [8–10]. These features make it well suited for storing and processing large amounts of data information in real time. In addition, the extensive range of materials available for the fabrication of resistive switching devices determines the unparalleled flexibility of memristor compared to other implantable devices. Currently, a series of works has been

devoted to explore the application of memristors in implantable devices. A memristor based on the Ag/CuMnO$_2$/Ti structure whose conductance values vary with the magnetic field levels is exhibited, demonstrating its potential application in health monitoring [11]. A number of polymer materials have also been used to fabricate memristor for implantable research, such as silver-doped PDMS, which maintains synaptic functionality even under 60 % strain and can perfectly composite on the surface of the organism or in vivo, which makes it prospective for use in implantable or wearable devices [12]. In addition to inorganic materials, organic materials have become the main focus in the fabrication of implantable memristor. Chen et al. [13]. prepared a non-volatile implantable memristor based on the Pt/AlOOH/ITO structure. The device achieved multi-resistive memristive characteristics and excellent biocompatibility. Compared with other biological memristor, the alooh-based memory resistor has a highly reliable multi-level resistive state, excellent environmental stability, and outstanding antioxidant performance, showcasing their excellent performance as implantable devices. Additionally, real-time monitoring and adaptive control of neuronal populations can be addressed by taking advantage of the fact that memristor can mimic synaptic behavior. Using the ex vivo hippocampal neuron cultures, a real-time adaptive control memristor system with a W/C + Ge$_2$Se$_2$/SnSe/Ge$_2$Se$_3$ Mix/Ag/Ge$_2$Se$_2$ Adhesion/W structure is showcased. This monitoring-computation-driving paradigm exhibits high reproducibility and could be envisioned for further application in automatic detection and inhibition of epileptic seizures in epilepsy patients [14]. However, the current application of memristors for biological health monitoring is limited and remains in the prospective stage, with no real biological implantation tests conducted yet.

Ferroelectric materials stand out among a host of functional layer materials due to their stable electrochemical properties as well as excellent ferroelectric properties [15–17]. BaTiO$_3$, as a typical ferroelectric material, exhibits excellent piezoelectric properties, as well as facile nano-synthesis and doping-modifiability. These characteristics make it highly suitable as a functional material for memristors [18–21]. However, it also suffers from a series of problems, the most fatal of which is that high dielectric losses and low Curie temperatures lead to reduced device durability, which is not conducive to long-term data storage and processing [22–24]. Reducing the dielectric loss and increasing the Curie temperature by doping the BaTiO$_3$ with oxides becomes an effective way to regulate the stability of BaTiO$_3$-based memristors [25–27]. On the other hand, among many oxides, MnO$_2$--based memristors have attracted widespread attention due to their excellent switching speed, superior magnetic field controllability, and high memristor stability [11,28,29]. The multiple valence states of the Mn element endow it with robust oxidizing and adsorption capacity. These distinctive properties position it as a pivotal candidate for modulating memristors [30,31].

In this work, a memristor with Ag/BaTiO$_3$/MnO$_2$/FTO structure was prepared, which exhibited excellent memristive stabilization properties. The first implantation study of this memristor in animals was conducted, as well as the implanted memristor in SD rats exhibited remarkable sensitivity to organismal information. Meanwhile, the memristive characteristics observed at three stages post-implantation highlighted the significant impact of voltage-driven organismal ions on memristive switching signals. Notably, reversible memristive switching behavior was achieved in implantable testing. This research demonstrates the feasibility of conducting implantable studies on memristors, showcasing their promising advantages for sensing applications in medical health monitoring, assisted diagnosis and treatment, as well as post-operative health recovery.

2. Experimental section

2.1. Devices preparation

A memristor featuring the Ag/BaTiO$_3$/MnO$_2$/FTO structure was fabricated using the magnetron sputtering method. Initially, a 0.1 mm thick, 20 × 20 mm^2 FTO sheet underwent polishing to eliminate surface oxides, followed by cleaning with ultra-pure water and ethyl alcohol. The BaTiO$_3$ and MnO$_2$ layers were deposited using magnetron sputtering, with a sputtering pressure of 0.7 Pa, sputtering power of 60 W, and sputtering time of 60 min. Finally, metal Ag was selectively deposited on the BaTiO$_3$ surface using a metal mask plate with 0.5 mm circular holes, employing magnetron sputtering at a pressure of 0.8 Pa, a power of 70 W, and a duration of 15 min.

2.2. Material characterization

Energy-dispersive X-ray spectroscopy spectrum (EDX spectrum) and mapping (EDX-mapping) were used to analyze deposited BaTiO$_3$ and MnO$_2$ thin film. The cross-section morphology of BaTiO$_3$ and MnO$_2$ was analyzed via scanning electron microscope (SEM). The electrochemical characteristics of memristor devices were characterized by employing keysight 2901B.

2.3. Animal experiments

The male Sprague-Dawley rat (8 weeks old) used in this study, purchased from the Experimental Animal Center of Xi'an Jiaotong University, was housed with a 12-h light/dark cycle and free access to water and chow. This study was approved by the Ethics Committee of the Animal Experiments of Xi'an Jiaotong University (XJTUAE2024-1547). The experimental protocol complied with the National Institutes of Health's Guide for the Care and Use of Laboratory Animals. The rat was weighed and then anesthetized with 1 % pentobarbital sodium solution (3 mL/kg) by intraperitoneal injection. The rat was fixed in the supine position, a median incision was made in its abdomen, and then a memristor was placed on the liver to detect the memristive effect. At the end of the experiment, the rat was euthanized by injecting air through the tail vein.

3. Results and discussion

The schematic diagram of the Ag/BaTiO$_3$/MnO$_2$/FTO device was presented in Fig. S1a, and SEM cross-section of the memristive device can be found in Fig. S1b, providing a clear depiction of the sandwich structure and the functional layers comprising BaTiO$_3$ (~320 nm) and MnO$_2$ (~206 nm). Fig. S1c depicts the EDX spectra of BaTiO$_3$ films, revealing the presence of Ba, Ti, and O elements. The corresponding weight percentages for these elements in the films are 23.43 %, 9.68 % and 66.89 %, respectively. Then, the existence of the BaTiO$_3$ and MnO$_2$ interface layer was reaffirmed using SEM-EDX elemental mapping based on elemental analysis of the functional layer interface, as shown in Figs. S1e–i. It can be observed that the titanium, copper, silver, barium, and oxygen elements exhibited a uniform distribution on the surface, aligning consistently with the EDX spectra. In addition, the resistance switching behavior is further analyzed when MnO$_2$ and BaTiO$_3$ at different thickness ratios, as shown in Fig. S2. Here, the thickness of the MnO$_2$ layer is fixed, and the film thickness ratio of MnO$_2$ and BaTiO$_3$ is adjusted by changing the thickness of the BaTiO$_3$ layer. It can be seen that the different ratios of thicknesses have not a huge influence on the memristive performance. However, the device exhibits a larger switching ratio about 6.3 when the thickness ratio of MnO$_2$ and BaTiO$_3$ is around 1:1.5, as shown in Fig. S2i-l. When the thickness ratio of MnO$_2$ is larger the device exhibits a better endurance. Besides, the retention properties of the memristive devices shows a significant decrease as the thickness ratio of BaTiO$_3$ increases, as shown in Fig. S2m-p. It can be seen that the variation of the thickness of MnO$_2$ and BaTiO$_3$ is not the main factor affecting the memristive performance.

It is well known that the implantable devices play a crucial role in patient health monitoring and postoperative diagnostic assistance. The integration of smart chips with sensing, storage, and arithmetic

capabilities in implantable research significantly accelerates the advancement of implantable devices [30–33]. Unlike previous device preparation means such as hot-melt extrusion, injection molding and 3D printing [34–37]. To determine the optimal scanning voltage range, the typical *I–V* curves are analyzed for six different voltage window ranges, where the arrow shows the sweep direction. Here, the 50th circle is selected for analysis, revealing minimal changes in memristor characteristics under increasing positive voltage. Notably, under the negative voltage range, the device displayed an optimal resistive switching window between −2.8 V and 2.8 V, as shown in Fig. S3. Further, it is analyzed the endurance performance under 100 cycles scanning, as shown in Fig. S4. Therefore, the −2.8 V–2.8 V loop scan range was selected to probe the memristor implantation test. The testing procedure is illustrated in Fig. 1. Initially, pre-implantation tests are conducted on the memristive device, subjecting it to memristance cycling tests exceeding 1300 cycles at a bias voltage ranging from −2.8 V to 2.8 V. Subsequently, the memristive device, connected with conductive wires, was implanted into the anesthetized abdominal cavity of SD rats. *I–V* cycle scanning tests are then performed at a bias voltage of −2.8 V–2.8 V. Finally, the memristive device is extracted, undergoes cleaning procedures, and it is reinstated for memristive performance testing under a bias voltage of −2.8 V–2.8 V.

The pre-implantation resistance switching performance of the memristor device is illustrated in Fig. 2. The schematic of the memristor with sandwich structure and the crystal structure of the functional layer are shown in Fig. 2a. Typical *I–V* curves above 1300 turns are demonstrated in Fig. 2b, where the arrows label the voltage sweep order. It can be found that the bias voltage of 0 V–2.8 V causes the device to initially remain in the high resistance state (HRS). Subsequently, the device undergoes a resistive transition from the HRS to the low resistance state (LRS) under a reverse voltage of 2.8 V to −1.8 V. Interestingly, the device conductance exhibits negative differential resistance (NDR) behavior at the bias voltage of −2.1 V to −2.8 V, which is mainly due to the migration of oxygen vacancies in the functional layer [38–41]. Fig. 2c illustrates the dynamic correlation between input and output signals. The peak output current is achieved when the chosen voltages in the positive and negative voltage regions reach approximately 2.8 V and −1.88 V, respectively. In the positive voltage range, currents and voltages exhibit temporal discrepancies, revealing asymmetric characteristics [42,43]. The *I–V* curves in logarithmic scale are demonstrated in Fig. 2d. The device always maintains in a LRS when the voltage shifts from positive bias to negative bias through 0 V, exhibiting a typical non-volatile behavior [44–46]. On the other hand, the SET process requires a positive voltage sweep, while RESET depends on a negative voltage sweep, indicating a typical bipolar resistance switching characteristic [47–49]. To further evaluate the performance of the memristive devices, endurance, retention, and statistical analysis are also performed. The cycle-to-cycle measurement above 1300 cycles demonstrate the robust endurance characteristic of Ag/BaTiO$_3$/MnO$_2$/FTO memristor as shown in Fig. 2e. The device stability and reliability are analyzed in Fig. 2f. It can be seen that there is a significant performance degradation of the memristive device at time scales. In addition, the HRS/LRS of the memristor show a tendency to become progressively smaller with the number of scanning turns, as shown in Fig. 2g. This is due to the fact that the Ag$^+$ of the upper electrode extend to the MnO$_2$ and BaTiO$_3$ under the positive voltage, which in turn reduces the effective thickness of the functional layer, leading to a decrease in the resistance value and a drop in the device retention characteristics. On the other hand, the oxygen vacancies in the functional layer are continuously depleted due to the constant scanning at 2.8 V to −2.8 V, which reduces the electron mobility and thus the device stability. However, it can be seen that the device becomes gradually stable after decreasing for a period of time. This is the result of the Ag ions continue to enter the functional layer with the scanning time, causing the resistance to gradually decrease. At the applied voltage amplitude of ±2.8 V, Ag ions can migrate into the MnO$_2$ and BaTiO$_3$ layer faster and reach saturation. Therefore, the device retention characteristics initially decrease with the sweeping cycle and then remain relatively stable. The HRS and LRS of the memristive device conforms to the Gaussian distribution as shown in Fig. 2h.

The mode of electron hopping between the BaTiO$_2$ and MnO$_2$ interfaces is analyzed based on fitting in different voltage regions. The work functions of the four materials (Ag ~ 4.26 eV [50], MnO$_2$ ~ 4.44 eV [51], BaTiO$_3$ ~ 4.0 eV [52], FTO ~ 4.6 eV [53]) are labeled in Fig. 3a. In the positive voltage region, the gradual increase in voltage causes the BaTiO$_3$ layer barrier to narrow, and the electron energy increases and hopping in the form of Fowler-Nordheim emission, as shown in Fig. 3b. The positive voltage continues to increase (1.2 V–2.8 V), causing the potential barrier difference between BaTiO$_3$ and MnO$_2$ to decrease, and the main conduction mechanism of electrons is hopping conduction, as shown in Fig. 3c. Due to the large number of electron leaps at this time, the device transforms from HRS to LRS. The higher voltage leads to a transient breakdown of the interface between MnO$_2$ and BaTiO$_3$, and the electron transition is mainly dominated by direct tunneling, as seen in Fig. 3d. When a small negative voltage is applied (−0 V to −2 V), although the barrier difference between the MnO$_2$ and BaTiO$_3$ interfaces increases, the energy barrier of MnO$_2$ and BaTiO$_3$ are narrow at this time, and electrons still have the ability to cross the barrier. Therefore, the transition mode of electrons at this stage is still mainly direct tunneling, as shown in Fig. 3e. As the negative voltage continues to increase (−2 V to −2.8 V), the barrier layers become thicker, causing the transition mode of electrons to change into Schottky emission, as shown in Fig. 3f.

Furthermore, the implantable testing on the Ag/BaTiO$_3$/MnO$_2$/FTO memristor aim to explore the sensitivity of memristive signals to biological environments. Here, SD rats are selected for intraperitoneal implantation of the memristor, and conductive wires through Ag wire at the top and bottom electrodes to facilitate testing, as shown in Fig. S6. Typical *I–V* curve of three stages at 20-turn intervals is depicted in Fig. S7. Fig. 4a shows the semi-log *I–V* curve performance of the Ag/BaTiO$_3$/MnO$_2$/FTO memristor with different sweeping cycles. The memristive window area of the device became significantly smaller as the device was continuous sweeping under bias voltage of −2.8 V–0 V — 2.8 V, indicating the biological tissue fluid of the SD rat caused a pretty dramatic effect on the memristive characters. To visualize this effect, the memristor device durability is analyzed by the distribution of HRS and LRS at a reading voltage of −0.12 V, as shown in Fig. 4b. It can be observed that the HRS and LRS shows phase changes with the sweep cycle at a reading voltage of −0.12 V, which can be mainly divide into three stages. In the first stage, the ratio of HRS/LRS is relatively large, and HRS and LRS present a better distinction between them. As the device is continuously swept, the resistive state of memristor reaches the second stage, i.e., the ratio of HRS/LRS decreases significantly, and the
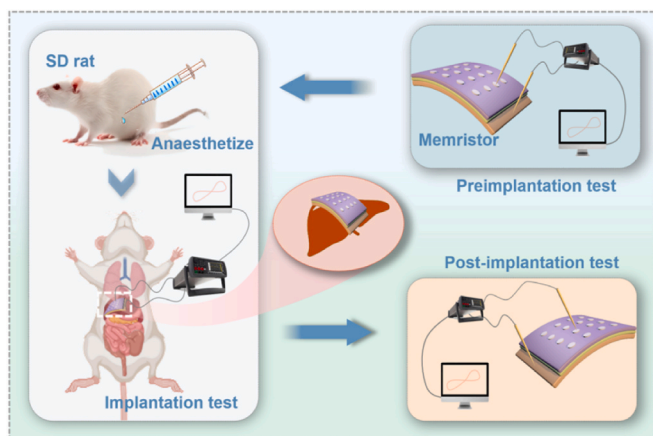

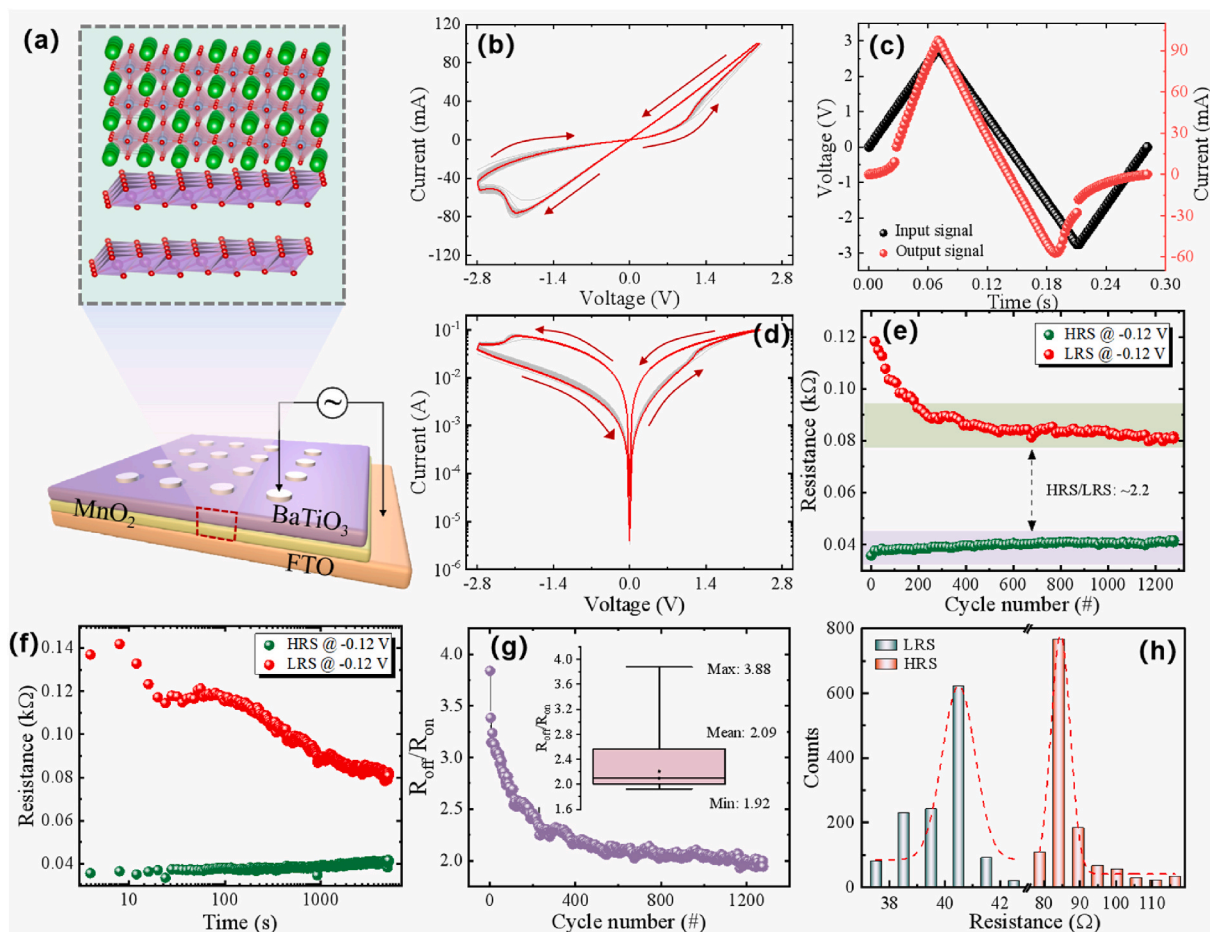**Fig. 1.** Schematic diagram of the implantable testing procedure.

Fig. 2. Pre-implantable testing of the Ag/BaTiO₃/MnO₂/FTO memristive device. (a) Schematic illustration of the Ag/BaTiO₃/MnO₂/FTO memristor. (b) Typical *I–V* curve of device under the sweeping voltage from 0 V → 2.8 V → 0 V→ −2.8 V → 0 V. (c) Temporal evolution curves of input and output signals. (d) The *I–V* curves on semi-log scale. (e) The HRS and LRS retention properties under 1300 cycles (f) Endurance measured more than 1000 s. (g) The functional relationship between HRS/LRS and switching cycle. (h) Gaussian distribution curve of HRS and LRS.
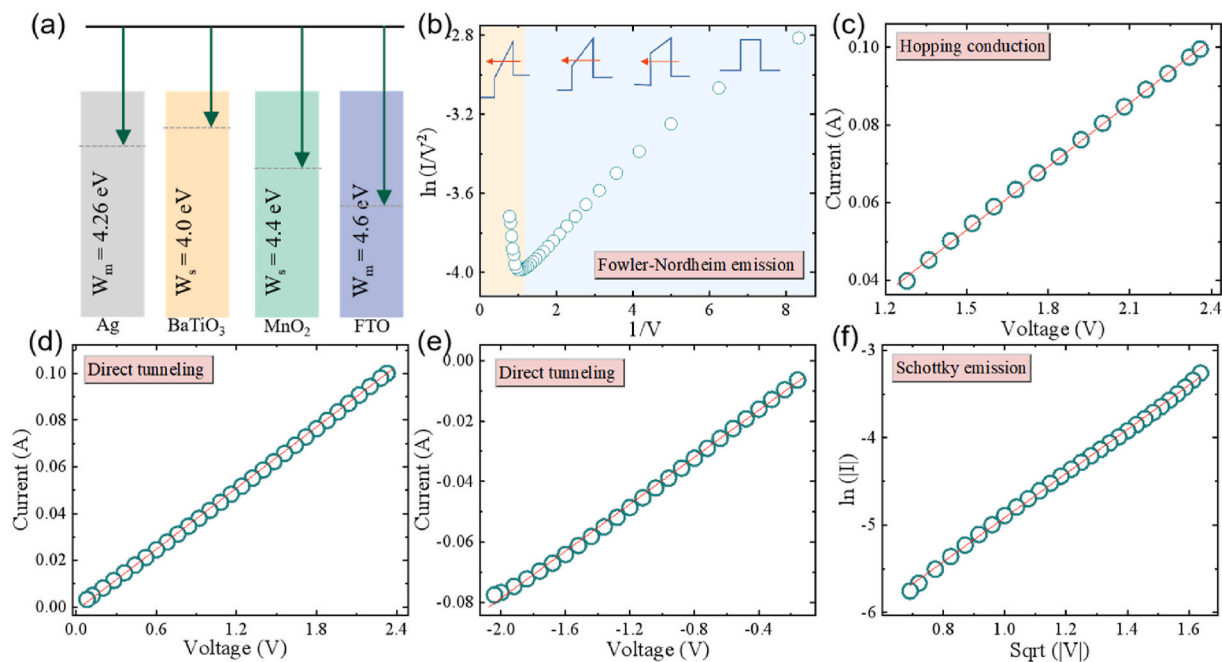

Fig. 3. Resistive switching mechanism under different voltage ranges through the data fitting. (a) The work function diagram of four materials. (b) Fowler-Nordheim emission, 0 V–1.3 V. (c) Hopping conduction, 1.3 V–2.3 V. (d) Direct tunneling, 2.3 V–0 V. (e) Direct tunneling, 0 V to −2 V. (f) Schottky emission, −2.7 V to −0.5 V.
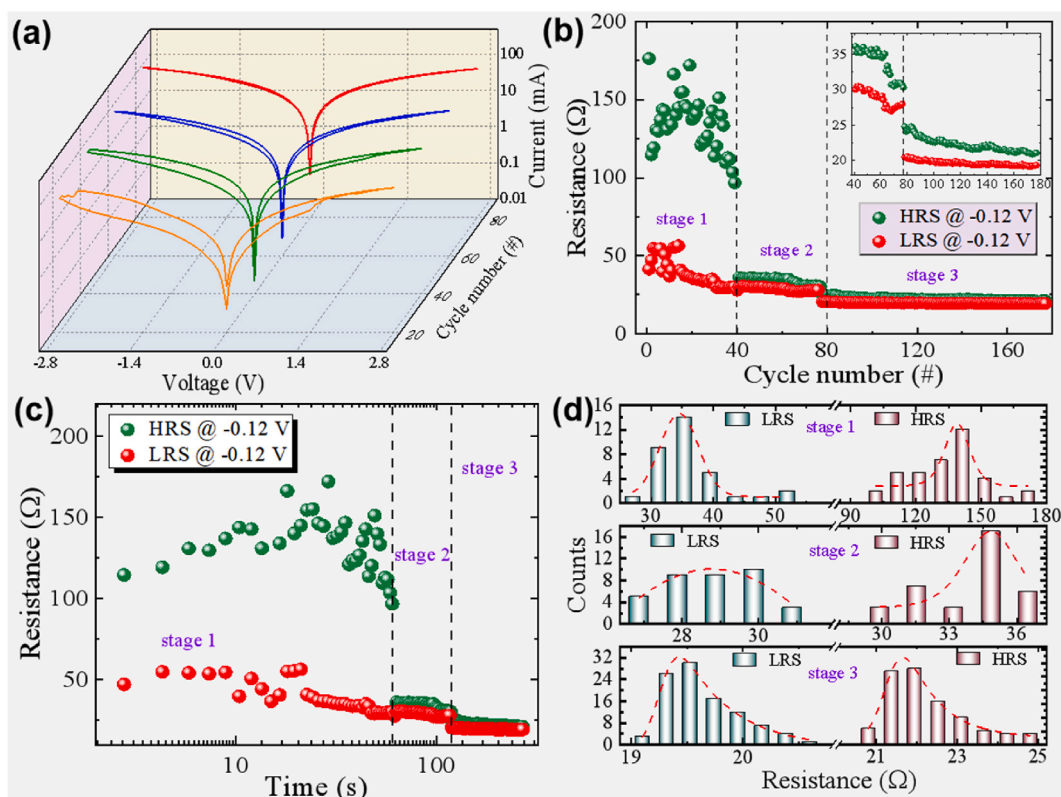
Fig. 4. Device implanted on liver surface for testing. (a) The semi-log *I–V* curve of three stages at 20-turn intervals. (b) The HRS and LRS retention properties under 180 cycles for tests with Ag/BaTiO₃/MnO₂/FTO memristor affixed to the surface of the liver. The insert is an enlarged view of stage 2 and stage 3. (c) Endurence measured of three stages more than 100 s. (d) Gaussian distribution for HRS and LRS in three stages.

resistive switching performance decays rapidly. After the 40 cycles of scanning, the resistive switching is gradually stabilized, and the memristive performance basically disappears. Fig. 4c shows the retention testing within three stages after device implantation in SD rats. It exhibits a similar effect to Fig. 4b, in which the retention performance shows stage changes with time.

Furthermore, the Gaussian distribution of the HRS and LRS are analyzed as shown in Fig. 4d, indicating there is a tendency toward a Gaussian distribution in stage 1 and stage 3. However, in stage 2, the resistance distribution does not align perfectly with a Gaussian distribution. This is due to the infiltration of body fluids around the electrode when the memristor is implanted into the SD rat. This phenomenon arises from the infiltration of body fluids around the electrode upon memristor implantation in SD rats. As bias voltage is applied, ions in the body fluids enter the functional layer driven by voltage, leading to distinct stages. In stage 1, a few ions impact memristor performance, causing fluctuations in HRS and LRS. With an increasing ion presence in stage 2, memristive behavior sharply declines, resulting in an unstable period where HRS and LRS poorly fit a Gaussian distribution. During stage 3, ions saturate the functional layer, stabilizing memristive device performance. Although HRS and LRS still adhere to a Gaussian distribution, the active involvement of ions significantly increases the conductivity of the functional layer, leading to the essential disappearance of memristive window.

Moreover, we conducted a deeper analysis of the reversibility by examining the resistive switching behavior of the memristor after it was removed from the external environment. The semi-log I–V curve demonstrates that the device undergoes periodic changes with scanning loops, as depicted in Fig. 5a. The typical I–V curves of the memristive devices as shown in Fig. S8, and Fig. 5b illustrates the endurance with 160 loops. During the initial 63 loops, the distinction between the HRS and LRS is minimal. Subsequently, a significant rise in the device's

switching ratio occurs, reactivating resistive switching and marking stage 2. The typical semi-log I–V curve of memristive device at different are shown in Fig. S9. Here, the memristive behavior in stage 2 is emphasized, ant the stability of the memristive device is analyzed, as depicted in Fig. 5c. The device exhibits robust stability for almost 100 s without noticeable performance degradation. Additionally, the distribution of HRS and LRS conforms to a Gaussian statistical pattern, as shown in Fig. 5d. It effectively demonstrates the outstanding reversibility of the memristive device post-implantation despite a modest switching ratio. Fig. 5e illustrates the alterations in the HRS and LRS of the memristor before and after implantation. It is evident that following implantation, the HRS of the test device is reduced compared to the initial state, while the LRS is increased. This phenomenon primarily stems from ions entering the functional layer during the implantation process under applied voltage, with crystal defect sites capturing some biological ions.

Despite undergoing voltage cycling tests for a certain period, these ions remain bound from BaTiO₃ and MnO₃, impacting the conductivity of memristor. The changes of HRS and LRS contribute to a specific attenuation of HRS/LRS ratio after device implantation, as depicted in Fig. 5f. Additionally, the current changes of the memristor before and after implantation at 2.8 V and −2.8 V are further analyzed, as depicted in Fig. 5g and h, respectively. It is noticeable that the current at the maximum negative voltage (−2.8 V) shows a slight increase compared to the initial state, though the magnitude is not substantial. Conversely, A distinct current increase is observed under post-implantation state at the maximum positive voltage (2.8 V). This suggests that the introduction of biological ions notably improves the conductivity of the functional layer, where Na⁺ and Cl⁻ identified as the primary ions contributing to degradation of memristive device. A more visual representation of the memristive performance changes is shown in Fig. 5i, where the performance decay is predominantly reflected in the
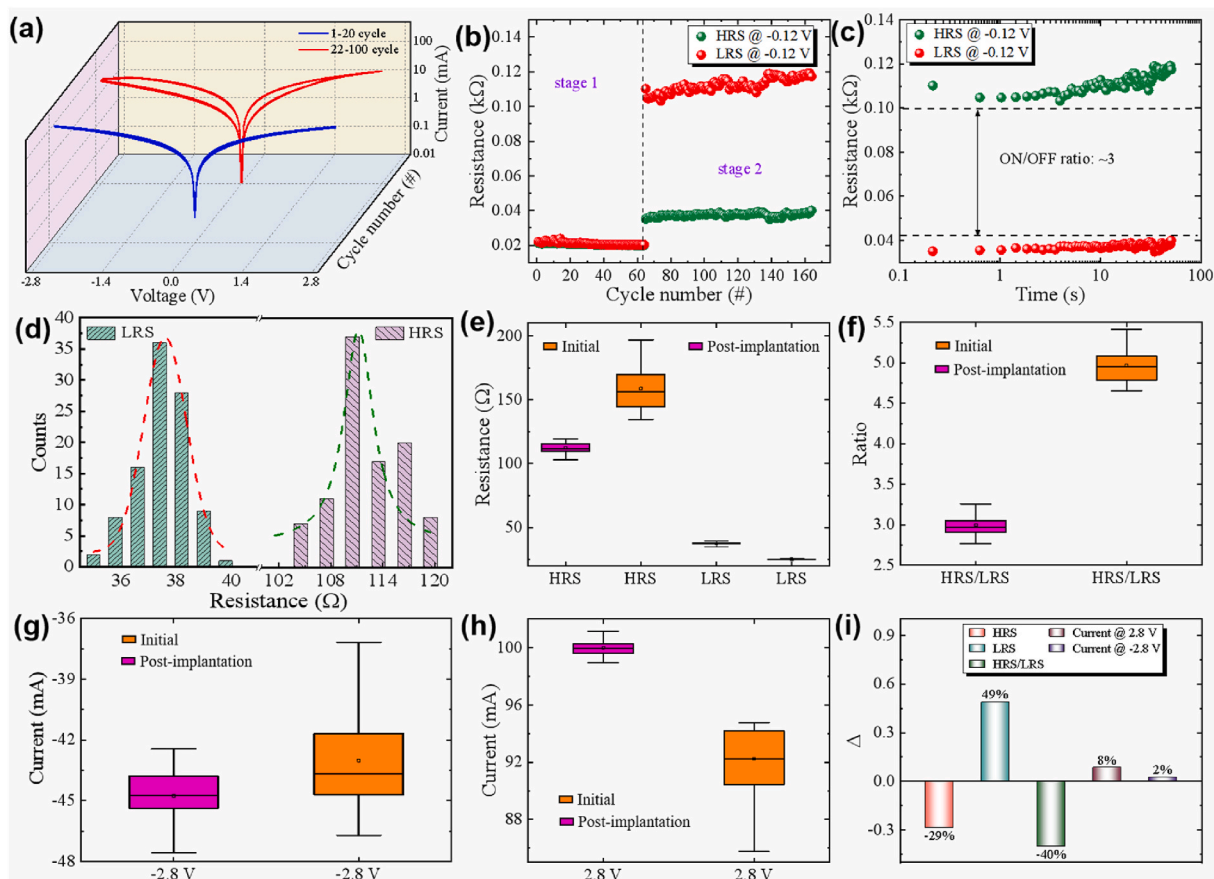
Fig. 5. Memristive characterization of the device after removal from the SD rat body. (a) The *I–V* curve with current on the logarithmic scale. (b) The HRS and LRS retention properties under two stages. (c) Endurance testing more than 1000 s. (d) Gaussian distribution for HRS and LRS. (e) Box plots illustrating the HRS and LRS performance changes in memristors after implantation compared to the initial state devices. (f) Box plots illustrating the HRS/LRS ratio changes after implantation compared to the initial state devices. (g) Compare the change in current values of memristors before and after implantation at applied voltage of −2.8 V. (h) Compare the change in current values of memristors before and after implantation at applied voltage of 2.8 V. (i) Memristor performance indicators decline before and after implantation. Where $\Delta = (X_{post-implantation} - X_{initial})/X_{post-implantation}$ ($X_{post-implantation}$ represents the current at ±2.8 V, HRS, LRS and HRS/LRS after implantation, $X_{initial}$ represents the corresponding values of the memristive device in its initial state.).

alterations of HRS and LRS. Post-implantation, the device exhibits a 49 % increase in LRS compared to the initial state and a 29 % decrease in HRS, marking the most direct impact on memristive performance.

Therefore, the as-prepared memristor exhibits significant sensitivity to biological information. Applying this highly sensitive implantable memristor to biomedical applications has the potential to achieve monitoring of biological signals [54,55]. This highlights the broad potential of implantable devices based on memristors in medical monitoring and diagnosis. On this basis, as shown in Fig. 6, an application program was designed to monitor blood supply during liver transplantation using a memristor. The migration of blood ions leads to significant changes in the conductivity of functional layer materials, which further affects the memristive behavior of implantable devices. Ultimately, real-time feedback was achieved, promoting real-time monitoring during liver transplantation.

4. Conclusions

In summary, a memristor with an Ag/BaTiO₃/MnO₂/FTO structure was successfully fabricated by employing magnetron sputtering. The as-prepared memristive device exhibited highly stable resistive switching behavior and demonstrated phased responses to biological signals upon implantation into SD rats. Notably, the device demonstrated remarkable reversibility after extraction from the rat, underscoring its significant potential for implantable health monitoring. This pioneering effort
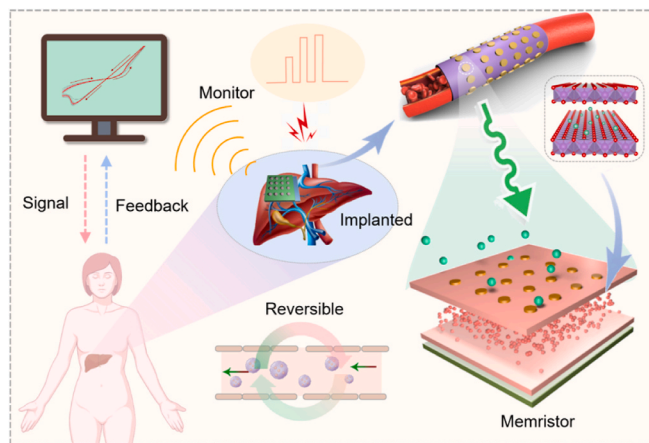

Fig. 6. A reversible and implantable memristor for hepatic transplantation blood supply monitoring.

represents the first implantation trial of a memristor, affirming its feasibility as a health monitoring device. Based on this, an implantable memristive device for functional monitoring of blood supply during liver transplantation is proposed. Furthermore, these findings provide valuable insights for future memristors applications of in biological

information detection, aiding diagnostics, and postoperative recovery monitoring.

CRediT authorship contribution statement

Zelin Cao: Writing – original draft, Investigation, Data curation. **Linbiao Xiang:** Methodology. **Bai Sun:** Writing – review & editing, Supervision, Funding acquisition. **Kaikai Gao:** Methodology. **Jiawei Yu:** Investigation. **Guangdong Zhou:** Formal analysis. **Xuegang Duan:** Formal analysis. **Wentao Yan:** Investigation. **Fulai Lin:** Methodology. **Zhuoqun Li:** Methodology. **Ruixin Wang:** Methodology. **Yi Lv:** Investigation. **Fenggang Ren:** Investigation. **Yingmin Yao:** Investigation. **Qiang Lu:** Supervision.

Declaration of competing interest

The authors declare that they have no known competing financial interests or personal relationships that could have appeared to influence the work reported in this paper.

Data availability

Data will be made available on request.

Acknowledgement

Appendix A. Supplementary data

Supplementary data to this article can be found online at https://doi.org/10.1016/j.mtbio.2024.101096.

References

[1] J.-A. Lee, Y.-G. Koh, K.-T. Kang, Biomechanical and clinical effect of patient-specific or customized knee implants: a review, J. Clin. Med. 9 (2020) 1559.

[2] N.J. Kamp, S.M. Al-Khatib, The subcutaneous implantable cardioverter-defibrillator in review, Am. Heart J. 217 (2019) 131–139.

[3] M.G. Crowson, Y.R. Semenov, D.L. Tucci, J.K. Niparko, Quality of life and cost-effectiveness of cochlear implants: a narrative review, Audiol. Neurootol. 22 (2017) 236–258.

[4] T. Hoffman, A. Khademhosseini, R. Langer, Chasing the paradigm: clinical translation of 25 years of tissue engineering, Tissue Eng. 25 (2019) 679–687.

[5] M. Dervisevic, M. Alba, B. Prieto-Simon, N.H. Voelcker, Skin in the diagnostics game: wearable biosensor nano-and microsystems for medical diagnostics, Nano Today 30 (2020) 100828.

[6] Y.J. Hong, H. Jeong, K.W. Cho, N. Lu, D.H. Kim, Wearable and implantable devices for cardiovascular healthcare: from monitoring to therapy based on flexible and stretchable electronics, Adv. Funct. Mater. 29 (2019) 1808247.

[7] F. Ali, S. El-Sappagh, S.R. Islam, A. Ali, M. Attique, M. Imran, K.S. Kwak, An intelligent healthcare monitoring framework using wearable sensors and social networking data, Future Generat. Comput. Syst. 114 (2021) 23–43.

[8] S. Chen, T. Zhang, S. Tappertzhofen, Y. Yang, I. Valov, Electrochemical-memristor-based artificial neurons and synapses-fundamentals, applications, and challenges, Adv. Mater. 35 (2023) 2301924.

[9] Z. Ma, W. Chen, X. Cao, S. Diao, Z. Liu, J. Ge, S. Pan, Criticality and neuromorphic sensing in a single memristor, Nano Lett. 23 (2023) 5902–5910.

[10] W. Zhang, P. Yao, B. Gao, Q. Liu, D. Wu, Q. Zhang, Y. Li, Z. Zhu, Y. Cai, D. Wu, J. Tang, H. Qian, Y. Wang, H. Wu, Edge learning using a fully integrated neuro-inspired memristor chip, Science 381 (2023) 1205–1211.

[11] S. Mao, B. Sun, G. Zhou, J. Qin, Y. Yang, Z. Rao, M. Liu, C. Ke, Z. Yong, A magnetic field controlled memristor towards the design of an implantable detector, J. Colloid Interface Sci. 643 (2023) 38–46.

[12] M. Yang, X. Zhao, Q. Tang, N. Cui, Z. Wang, Y. Tong, Y. Liu, Stretchable and conformable synapse memristors for wearable and implantable electronics, Nanoscale 10 (2018) 18135.

[13] X. Chen, X. Zhao, X. Huang, X.-Z. Tang, Z. Sun, D.-L. Ni, H. Hu, J. Yue, Flexible multilevel nonvolatil biocompatible memristor with high durability, J. Nanobiotechnol. 21 (2023) 375.

[14] C. Dias, D. Castro, M. Aroso, J. Ventura, P. Aguiar, Memristor-based neuromodulation device for real-time monitoring and adaptive control of neuronal populations, ACS Appl. Electron. Mater. 4 (2022) 2380–2387.

[15] J.M. Yan, J.S. Ying, M.Y. Yan, Z.C. Wang, S.S. Li, T.W. Chen, G.Y. Gao, F.Y. Liao, H. S. Luo, T. Zhang, Y. Chai, R.-K. Zheng, Optoelectronic coincidence detection with two-dimensional Bi_2O_2Se ferroelectric field-effect transistors, Adv. Funct. Mater. 31 (2021) 2103982.

[16] T. Mikolajick, M.H. Park, L. Begon-Lours, S. Slesazeck, From ferroelectric material optimization to neuromorphic devices, Adv. Mater. 35 (2023) 2206042.

[17] Z. Gao, Y. Wang, Z. Lv, P. Xie, Z. Xu, M. Luo, Y. Zhang, S. Huang, K. Zhou, G. Zhang, G. Duan, Y. Zhou, S.-T. Han, Ferroelectri coupling for dual-mode non-filamentary memristors, Appl. Phys. Rev. 9 (2022) 021417.

[18] T. Das, P. Biswas, A. Dev, J. Mallick, M. Kar, Multi-functional piezoelectric nanogenerator based on relaxor ferroelectric materials (BSTO) and conductive fillers (MWCNTs) for self-powered memristor and optoelectronic devices, Chem. Eng. J. 479 (2024) 147900.

[19] X. Yan, H. He, G. Liu, Z. Zhao, Y. Pei, P. Liu, J. Zhao, Z. Zhou, K. Wang, H. Yan, A robust memristor based on epitaxial vertically aligned nanostructured $BaTiO_3$-CeO_2 films on silicon, Adv. Mater. 34 (2022) 2110343.

[20] C. Ma, Z. Luo, W. Huang, L. Zhao, Q. Chen, Y. Lin, X. Liu, Z. Chen, C. Liu, H. Sun, X. Jin, Y. Yin, X. Li, Sub-nanosecond memristor based on ferroelectric tunnel junction, Nat. Commun. 11 (2020) 1439.

[21] A. Molinari, R. Witte, K.K. Neelisetty, S. Gorji, C. Kübel, I. Münch, F. Wöhler, L. Hahn, S. Hengsbach, K. Bade, H. Hahn, R. Kruk, Configurable resistive response in $BaTiO_3$ ferroelectric memristors via electron beam radiation, Adv. Mater. 32 (2020) 1907541.

[22] B. Luo, X. Wang, E. Tian, H. Song, Q. Zhao, Z. Cai, W. Feng, L. Li, Giant permittivity and low dielectric loss of fe doped $BaTiO_3$ ceramics: experimental and first-principles calculations, J. Eur. Ceram. Soc. 38 (2018) 1562–1568.

[23] D. He, Y. Wang, X. Chen, Y. Deng, Core-shell structured $BaTiO_3@Al_2O_3$ nanoparticles in polymer composites for dielectric loss suppression and breakdown strength enhancement, Compos. Part A-appl S. 93 (2017) 137–143.

[24] Z. Lv, J. Wei, T. Yang, Z. Sun, Z. Xu, Manipulation of curie temperature and ferroelectric polarization for large electrocaloric strength in $BaTiO_3$-based ceramics, Ceram. Int. 46 (2020) 14978–14984.

[25] J.H. Yoon, Z.R. Wang, K.M. Kim, H.Q. Wu, V. Ravichandran, Q.F. Xia, C.S. Hwang, J.J. Yang, An artificial nociceptor based on a diffusive memristor, Nat. Commun. 9 (2018) 417.

[26] X. Yan, X. Yan, G. Liu, J. Zhao, Z. Zhao, H. Wang, H. He, M. Hao, Z. Li, L. Wang, W. Wang, Z. Jian, J. Li, J. Chen, Silicon-based epitaxial ferroelectric memristor for high temperature operation in self-assembled vertically aligned $BaTiO_3$-CeO2 films, Nano Res. 15 (2022) 9654–9662.

[27] V. Paunovic, V.V. Mitic, M. Djordjevic, Z. Prijic, Niobium doping effect on $BaTiO_3$ structure and dielectric properties, Ceram. Int. 46 (2020) 8154–8164.

[28] S. Mao, B. Sun, Y. Yang, J. Wang, H. Zhao, Y. Zhao, α-MnO_2 nanorods-based memristors with nonvolatile resistive switching behavior, Ceram. Int. 48 (2022) 32860–32866.

[29] W. Zhao, F. Xu, L. Liu, M. Liu, B. Weng, Strain-induced electronic structure modulation on MnO_2 nanosheet by Ir incorporation for efficient water oxidation in acid, Adv. Mater. 35 (2023) 2308060.

[30] R. Yang, Y. Fan, R. Ye, Y. Tang, X. Cao, Z. Yin, Z. Zeng, MnO_2-based materials for environmental applications, Adv. Mater. 33 (2021) 2004862.

[31] Y. Zhou, M. Li, T. Zhang, Y. Chen, X. Li, H. Jia, P. Xu, X. Li, Cooperative characterization of in situ TEM and cantilever-TGA to optimize calcination conditions of MnO_2 nanowire precursors, Nano Lett. 23 (2023) 2412–2420.

[32] M. Hassan, G. Abbas, N. Li, A. Afzal, Z. Haider, S. Ahmed, X. Xu, C. Pan, Z. Peng, Significance of flexible substrates for wearable and implantable devices: recent advances and perspectives, Adv. Mater. Technol-US 7 (2022) 2100773.

[33] A. Kar, N. Ahamad, M. Dewani, L. Awasthi, R. Patil, R. Banerjee, Wearable and implantable devices for drug delivery: applications and challenges, Biomaterials 283 (2022) 121435.

[34] M. Pal, K.M. Subhedar, CNT yarn-based solid-state linear supercapacitor with multi-featured capabilities for wearable and implantable devices, Energy Storage Mater. 57 (2023) 136–170.

[35] M.F. Simões, R.M.A. Pinto, S. Simões, Hot-melt extrusion in the pharmaceutical industry: toward filing a new drug application, Drug Discov. Today 24 (2019) 1749–1768.

[36] P. Zhao, J. Zhang, Z. Dong, J. Huang, H. Zhou, J. Fu, L. Turng, Intelligent injection molding on sensing, optimization, and control, Adv. Polym. Technol. 2020 (2020) 1–22.

[37] J.P. Camila, J. Domínguez-Robles, E. Utomo, A.J. Paredes, F. Volpe-Zanutto, D. Malinova, R.F. Donnelly, E. Larrañeta, 3D-printed implantable devices with biodegradable rate-controlling membrane for sustained delivery of hydrophobic drugs, Drug Deliv. 29 (2022) 1038–1048.

[38] X. Hu, W. Wang, B. Sun, Y. Wang, J. Li, G. Zhou, Refining the negative differential resistance effect in a TiO_x-based memristor, J. Phys. Chem. Lett. 21 (2021) 5377–5383.

[39] S. Mao, B. Sun, C. Ke, J. Qin, Y. Yang, T. Guo, Y. Wu, J. Shao, Y. Zhao, Evolution between CRS and NRS behaviors in $MnO_2@TiO_2$ nanocomposite-based memristor for multi-factors-regulated memory application, Nano Energy 107 (2023) 108117.

[40] V. Humbert, R.E. Hage, G. Krieger, G. Sanchez-Santolino, A. Sander, S. Collin, J. Trastoy, J. Briatico, J. Santamaria, D. Preziosi, J.E. Villegas, An oxygen vacancy memristor ruled by electron correlations applications, Adv. Sci. 9 (2022) 2201753.

[41] C. Yang, B. Sun, G. Zhou, T. Guo, C. Ke, Y. Chen, J. Shao, Y. Zhao, H. Wang, Photoelectric memristor-based machine vision for artificial intelligence applications, ACS Mater. Lett. 5 (2023) 504–526.

[42] H. Zhang, B. Jiang, C. Cheng, B. Huang, H. Zhang, R. Chen, J. Xu, Y. Huang, H. Chen, W. Pei, Y. Chai, F. Zhou, A Self-rectifying synaptic memristor array with ultrahigh weight potentiation linearity for a self-organizing-map neural network, Nano Lett. 23 (2023) 3107–3115.

[43] T. Guo, J. Ge, B. Sun, K. Pan, Z. Pan, L. Wei, Y. Yan, Y.N. Zhou, Y.A. Wu, Soft biomaterials-based flexible artificial synapse for neuromorphic computing, Adv. Electron. Mater. 8 (2022) 2200449.

[44] W. Park, G. Kim, J.H. In, H. Rhee, H. Song, J. Park, A. Martinez, K.M. Kim, High amplitude spike generator in Au nanodot-incorporated NbO_x Mott memristor, Nano Lett. 23 (2023) 5399–5407.

[45] Z. Cao, B. Sun, G. Zhou, S. Mao, S. Zhu, J. Zhang, C. Ke, Y. Zhao, J. Shao, Memristor-based neural networks: a bridge from device to artificial intelligence, Nanoscale Horiz 8 (2023) 716–745.

[46] X.F. Lu, Y. Zhang, N. Wang, S. Luo, K. Peng, L. Wang, H. Chen, W. Gao, X.H. Chen, Y. Bao, G. Liang, K.P. Loh, Exploring low power and ultrafast memristor on p-type van der Waals SnS, Nano Lett. 21 (2021) 8800–8807.

[47] Z. Cao, B. Sun, S. Mao, G. Zhou, X. Duan, W. Yan, S. Sun, X. Chen, J. Shao, Controllable analog-to-digital bipolar resistive switching behavior and mechanism analysis in δ-MnO_2-based memristor, Mat. Today Phys. 38 (2023) 101264.

[48] L. Yin, R. Cheng, Z. Wang, F. Wang, M.G. Sendeku, Y. Wen, X. Zhan, J. He, Two-dimensional unipolar memristors with logic and memory functions, Nano Lett. 20 (2020) 4144–4152.

[49] C.P. Singh, V.P. Singh, H. Ranjan, S.K. Pandey, Bipolar and rectifying resistive switching dynamics in e-beam evaporated SnO_x based memristor, Ceram. Int. 50 (2024) 4092–4100.

[50] C. Beasley, M.K. Gnanamani, E. Santillan-Jimenez, M. Martinelli, W.D. Shafer, S. D. Hopps, N. Wanninayake, D.-Y. Kim, Effect of metal work function on hydrogen production from photocatalytic water splitting with $MTiO_2$ catalysts, ChemistrySelect 5 (2020) 1013–1019.

[51] J. Chang, M. Jin, F. Yao, T.H. Kim, V.T. Le, H. Yue, F. Gunes, B. Li, A. Ghosh, S. Xie, Y.H. Lee, Asymmetric supercapacitors based on graphene/MnO_2 nanospheres and graphene/MoO_3 nanosheets with high energy density, Adv. Funct. Mater. 23 (2013) 5074–5083.

[52] G. Panthi, M. Park, Approaches for enhancing the photocatalytic activities of barium titanate: a review, J. Energy Chem. 73 (2022) 160–188.

[53] H. Sun, Y. Zhou, Y. Xin, K. Deng, L. Meng, J. Xiong, L. Li, Composition and energy band-modified commercial FTO substrate for in situ formed highly efficient electron transport layer in planar perovskite solar cells, Adv. Funct. Mater. 29 (2019) 1808667.

[54] J. Zhang, J. Du, C. Yang, H. Liang, Z. Cao, X. Duan, W. Yan, Y. Zhao, B. Sun, Memristor based electronic devices towards biomedical applications, J. Mater. Chem. C 12 (2024) 50–59.

[55] B. Sun, Y. Chen, G. Zhou, Z. Cao, C. Yang, J. Du, X. Chen, J. Shao, Memristor-based artificial chips, ACS Nano 18 (2024) 14–27.